JGR Solid Earth

RESEARCH ARTICLE
10.1029/2020JB020513

# Autocorrelation Infrasound Interferometry

**Hugo D. Ortiz[1,2], Robin S. Matoza[1], Jeffrey B. Johnson[3], Stephen Hernandez[4], Juan C. Anzieta[2], and Mario C. Ruiz[4]**

[1]Department of Earth Science and Earth Research Institute, University of California, Santa Barbara, CA, USA, [2]Facultad de Ciencias Exactas y Naturales, Pontificia Universidad Católica del Ecuador, Quito, Ecuador, [3]Department of Geosciences, Boise State University, ID, USA, [4]Instituto Geofísico, Escuela Politécnica Nacional, Quito, Ecuador

**Key Points:**

- Relative velocity changes derived from infrasound autocorrelations can track independently observed temperature and wind variations
- Autocorrelation infrasound interferometry can take advantage of high-frequency persistent infrasound noise sources, such as waterfalls
- We demonstrate the applicability of autocorrelation infrasound interferometry for a range of geographical locations and station designs

**Supporting Information:**

Supporting Information may be found in the online version of this article.

**Correspondence to:**

H. D. Ortiz,
hdortiz@ucsb.edu;
hdortiz@puce.edu.ec

**Citation:**

Ortiz, H. D., Matoza, R. S., Johnson, J. B., Hernandez, S., Anzieta, J. C., & Ruiz, M. C. (2021). Autocorrelation infrasound interferometry. *Journal of Geophysical Research: Solid Earth*, *126*, e2020JB020513. https://doi.org/10.1029/2020JB020513

Received 8 JUL 2020
Accepted 22 FEB 2021



**Abstract** Seismic and infrasound multistation ambient-noise interferometry has been widely used to infer ground and atmospheric properties, and single-station and autocorrelation seismic interferometry has also shown potential for characterizing Earth structure at multiple scales. We extend autocorrelation seismic interferometry to ambient atmospheric infrasound recordings that contain persistent local noise from waterfalls and rivers. Across a range of geographic settings, we retrieve relative sound-speed changes that exhibit clear diurnal oscillations consistent with temperature and wind variations. We estimate ambient air temperatures from variations in relative sound speeds. The frequency band from 1 to 2 Hz appears most suitable to retrieve weather parameters as nearby waterfalls and rivers may act as continuous and vigorous sources of infrasound that help achieve convergence of coherent phases in the autocorrelation codas. This frequency band is also appropriate for local sound-speed variations because it has infrasound with wavelengths of ~170–340 m, corresponding to a typical atmospheric boundary layer height. After applying array analysis to autocorrelation functions derived from a three-element infrasound array, we find that autocorrelation codas are composed of waves reflected off nearby topographic features, such as caldera walls. Lastly, we demonstrate that autocorrelation infrasound interferometry offers the potential to study the atmosphere over at least several months and with a fine time resolution.

**Plain Language Summary** Atmospheric infrasound is sound waves with frequencies less than the 20 Hz human hearing threshold. Infrasound sensors are being increasingly deployed to monitor volcanoes, streams, ocean wave activity, thunder, snow avalanches, meteorites, and anthropogenic explosions. Here, we present a new technique to analyze background noise recorded by infrasonic sensors to extract atmospheric sound-speed perturbations, which in turn can be used to infer air temperature and wind velocity variations. We show that the infrasound inferred temperature changes recovered by this method track closely with independently measured temperature cycles. This method may be useful for exploiting existing infrasound networks to provide long time series of atmospheric temperature fluctuations and increasing the spatial density of ground-based thermometry.

## 1. Introduction

Through laboratory experiments, Weaver and Lobkis (2001, 2002) showed that autocorrelations and cross correlations of ultrasonic noise records can be used to obtain the Green's functions of a medium. Subsequently, these concepts were applied to seismic records by Campillo and Paul (2003) and Shapiro and Campillo (2004), who demonstrated that cross correlations of seismic codas and noise, respectively, can be used to obtain the response of the Earth. Similar developments took advantage of incoherent ambient noise in the ocean to obtain coherent acoustic wave fronts between hydrophones (Roux & Kuperman, 2004) and to determine water depth and seabed subbottom layering (Siderius et al., 2006). Later, Sens-Schönfelder and Wegler (2006) introduced passive image interferometry, which consists of applying coda wave interferometry (Snieder et al., 2002) to the tails of the passively retrieved Green's functions to quantify relative velocity changes of the medium. Passive image interferometry is commonly applied to Green's functions derived from a single sensor or a pair of sensors. Here, we present a method that builds upon coda wave interferometry applied to Green's functions inferred from autocorrelations of (single-sensor) infrasound (atmospheric acoustics <20 Hz) records.

Seismic interferometry exploits ambient seismic noise to infer the Green's function of the subsurface, a proxy for the Earth's response (Campillo & Paul, 2003; Shapiro & Campillo, 2004; Wapenaar et al., 2010).

This technique has proven effective for the recovery of solid Earth structure at multiple spatiotemporal scales, including mapping faults (Brenguier et al., 2019; Wegler & Sens-Schönfelder, 2007) and inferring time variations in volcanic structure (Brenguier et al., 2008). While seismic noise can be of natural or anthropogenic origin (Bonnefoy-Claudet et al., 2006), interferometry studies mainly use microseismic noise because it is ubiquitous on Earth and generally provides good azimuthal sampling of the medium. Microseisms have periods of ~5–8 s and are generated by stationary ocean waves that result from opposing wave–wave superposition (Longuet-Higgins, 1950). Microseisms are stronger at the shore and their power decreases with distance from the shore. Their atmospheric counterparts, microbaroms, are also generated by ocean wave–wave interactions and have peak frequencies of ~0.12–0.35 Hz (Donn & Rind, 1972; Waxler & Gilbert, 2006). Since infrasound atmospheric attenuation is low, microbaroms can propagate thousands of kilometers, making them also ubiquitous on Earth (Landès et al., 2012; Matoza et al., 2013).

Microbaroms recorded at two or more infrasound sensors have been used to investigate sound-speed changes in the troposphere. Haney (2009) used two infrasound sensors separated 13.5 km during 1 day to obtain hourly sound-speed vertical profiles, from the ground to 4 km. Fricke et al. (2014) used a large aperture (82.6 km) array to get the direction of arrival of microbaroms and the effective sound speed at the ground surface for a period of 10 days. Here, we demonstrate that autocorrelation functions from a single infrasound sensor can also provide information on daily variations of the (atmospheric) sound speed near to the sensor. We show that low-frequency variations of the relative velocity change can track independently measured temperature and wind cycles.

The ability to infer atmospheric sound-speed variations with a single infrasound sensor may offer several potential advantages over multistation methods (e.g., Fricke et al., 2014; Haney, 2009). For example, it avoids needing to consider station pairs where convergence of the Green's functions is difficult to attain (e.g., Fricke et al., 2014), or when a sensor malfunction voids information from the cross-correlation pair. We show that single-sensor interferometry offers the potential to measure the atmosphere continuously over long time scales (at least several months in this study) and with a fine time resolution (~34 min). Furthermore, single-sensor methods may permit using sparser sensor networks in infrasound interferometry to help complement available atmospheric observation systems.

## 2. Data and Infrasound Sources

### 2.1. Infrasound at El Reventador

Since 2015, Pontificia Universidad Católica del Ecuador, Boise State University, and Escuela Politécnica Nacional have progressively installed three temporary infrasound arrays close to El Reventador volcano (Volcán El Reventador; −0.078°, −77.656°), Ecuador: AZU, LAV, and CON (Figure 1). AZU and LAV were installed in January 2015 and CON was installed in September 2018. The arrays are located at distances ranging from 2.2 to 3.9 km from the summit and have apertures between 24 and 81 m (Figure 1b and 1c). The temporary deployments are supplemented by a permanent infrasound station, REVS, installed in early 2013. The arrays are composed of three InfraBSU microphones (Marcillo et al., 2012) connected to 24-bit REF TEK 130 digitizers until August 2017 and then to 24-bit DATA-CUBE digitizers, sampling at 100 Hz (Figure 1c). Permanent station REVS has a single MB2005 microbarometer connected to a Quanterra Q330 digitizer sampling at 50 Hz. InfraBSU microphones have a dynamic range of ±125 Pa and a flat response from 0.05 to 50 Hz, whereas the MB2005 sensor has a dynamic range of ±8,000 Pa and a flat response from 0.01 to 27 Hz.

The main infrasound sources detected and reported in the area correspond to Volcán El Reventador and nearby San Rafael waterfall (Figures 2 and S1); however, there are detections from other sources such as microbaroms, thunder, and streams (e.g., Johnson, 2006; Johnson et al., 2006; Ortiz et al., 2019). Detections in 2019 show that the infrasound wavefield is produced by multiple sources in the region and that the superposition of these sources likely contributes to the overall broadband “noise” (which includes coherent infrasound signals) that is utilized in the interferometry procedure (Figure 2a). For example, detections at the CON array show that persistent infrasound from El Reventador (243°) and San Rafael (110°) are accompanied by additional low-frequency (<1 Hz) and high-frequency signals (~7–10 Hz).

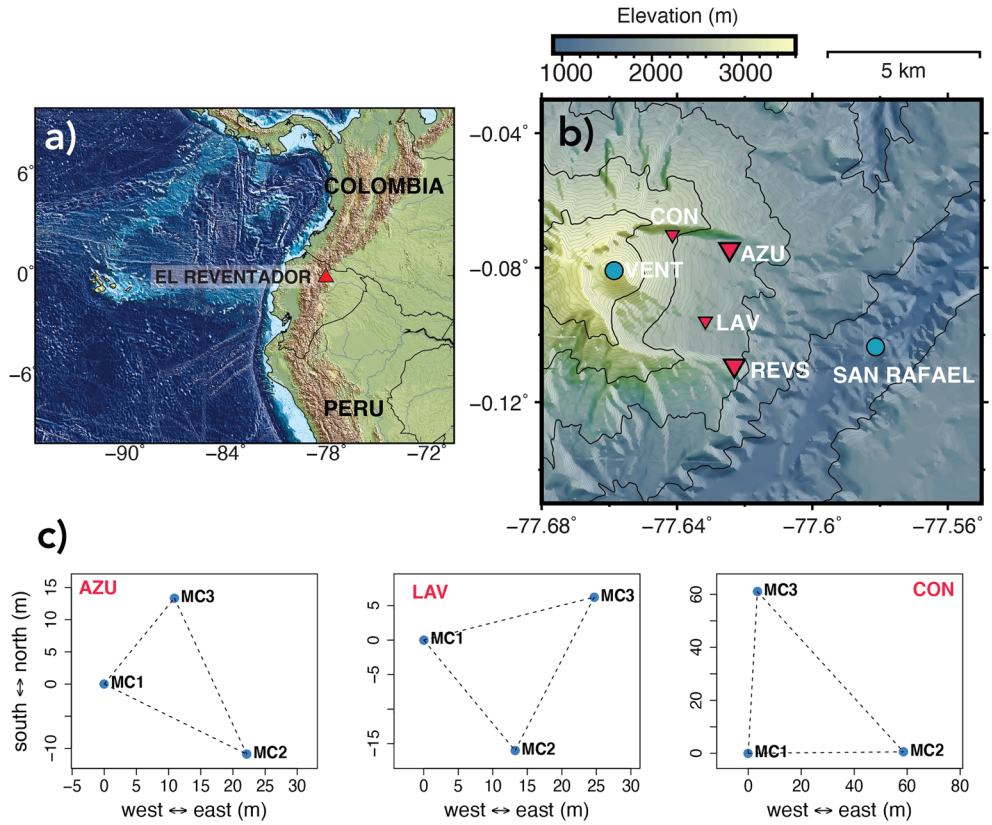


**Figure 1.** Network of infrasound arrays deployed at Volcán El Reventador. (a) Volcán El Reventador is in the Eastern Cordillera of Ecuador near to the border with Colombia. (b) Locations of sensors (red triangles) and persistent infrasound sources (blue dots). Continuous infrasound recordings start in 2013 from the single sensor station REVS (2013 to present) and later from LAV (2015 to present), AZU (2015 to present), and CON (2018 to present) infrasound arrays. (c) The geometries for AZU, LAV, and CON infrasound arrays have apertures of 25, 24, and 81 m, respectively.

The low-frequency (<1 Hz) signals are likely microbaroms originating in the Pacific Ocean as they have back azimuths of ~260°–320° and their frequencies are consistent with microbaroms reported in other regions (e.g., Donn & Rind, 1972; Matoza et al., 2013; Ortiz et al., 2020). The high-frequency (~7–10 Hz) signals could be thunder, as they only last for short time periods and have variable back azimuths, which are common features of thunder (Johnson et al., 2011). Although the back azimuth resolution is lower at AZU, since 2015, we also identify El Reventador and San Rafael as the most prominent sources of infrasound (Figure S1). For back azimuth detection and characterization, we use the Progressive Multi-Channel Correlation method (PMCC; Cansi, 1995) with 30 log-spaced frequency bands and time-window lengths (Figure 2d).

### 2.2. Additional Data Specifications

We use all three channels (separately) from the AZU array and microphone #1 from LAV array to illustrate the interferometry method. We then apply a similar procedure to data from REVS and stations P30M, R32K, and H17A from the EarthScope Transportable Array (TA) (Figure S2). We consider these additional stations to investigate the robustness of the methodology for different station configurations and geographical locations as well as to compare interferometry results with temperature and wind observations from dedicated sensors. Parameters such as filter specification, decimation factors, and time-window lengths were adapted for each station and are detailed in the supporting information along with additional technical information.

We emphasize that even though AZU and LAV are infrasound arrays (have three infrasound sensors), we present here an autocorrelation interferometry method that uses only a single infrasound sensor at a time.

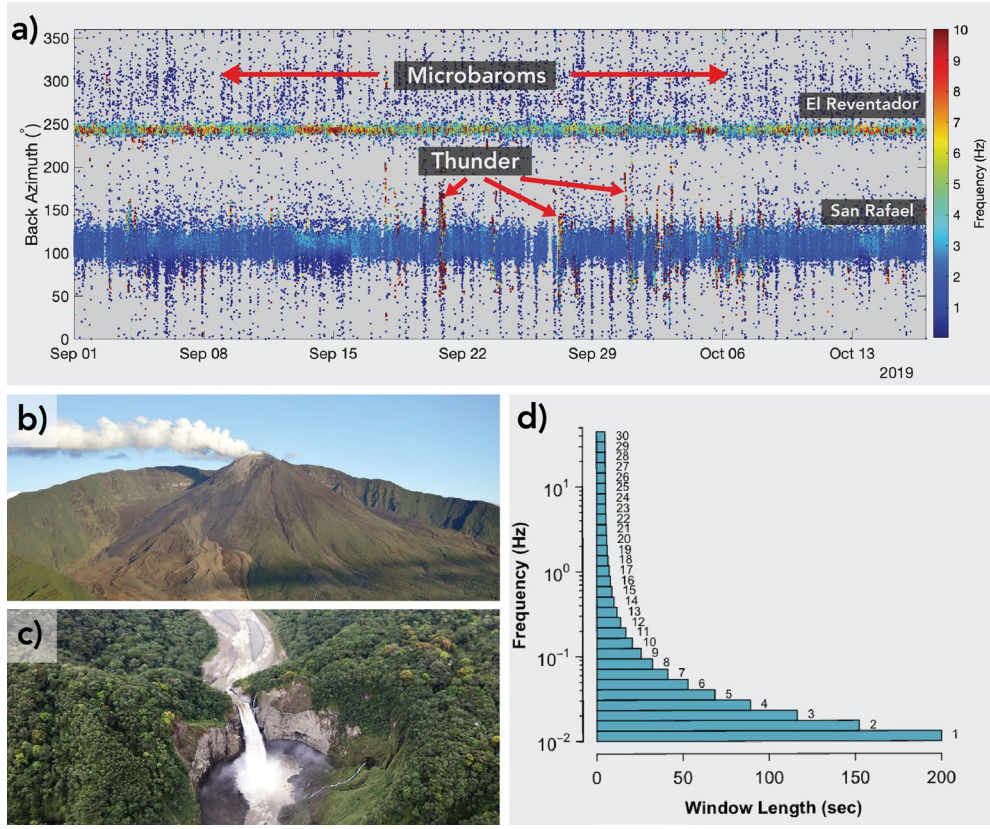


**Figure 2.** PMCC back azimuths of infrasound sources recorded in El Reventador's proximity. (a) Back azimuths detections at CON array show Volcán El Reventador (243°), San Rafael waterfall (110°), microbaroms (~260°–320°), and occasional thunder signals, which have high frequencies (~7–10 Hz) and variable back azimuths. Detections span from September 1 to October 16, 2019. (b) El Reventador as seen from the southeast shows a continuous degassing plume moving toward the west. Photo courtesy of Steve Schilling. (c) San Rafael falls had a total vertical water drop of 145 m and discharge of up to 500 $m^3/s$ (Johnson, 2006). However, on February 2, 2020, the waterfall disappeared after a natural collapse as reported by the Ecuadorian Minister of the Environment. (d) Detail of the 30 log-space frequency bands and time-windows used in PMCC. Time-windows are consecutive and overlapped 90%. PMCC, Progressive Multi-Channel Correlation method.

We analyze infrasound data recorded between January 14 and July 22, 2015, because of the relative quiescence of Volcán El Reventador, which is located 3.9 km from AZU and 3.4 km from LAV. The microphones are separated by about 14 m from each digitizer, which are inside a plastic box (vault). As part of their state-of-health operations, the REF TEK 130 digitizers also log ambient air temperature (inside the vault) every hour with a temperature resolution of 1°C. There are no wind data near El Reventador.

## 3. Methods

### 3.1. Autocorrelation Functions

First, we filter the 1-day files between 1 and 2 Hz using a fourth-order Butterworth filter because most of the acoustic energy near El Reventador is focused in this frequency band (Figure 4a). Next, we decimate the infrasound traces to 50 Hz and apply 1-bit normalization (e.g., Bensen et al., 2007). Spectral whitening is not applied to the traces as this would have the effect of converting autocorrelation functions into approximate delta functions that do not contain information on the medium velocity (Hobiger et al., 2014). Finally, we divide 1-day files into 2,048-s windows overlapped 50% and then corresponding windows are autocorrelated following the Wiener–Khinchin theorem in the frequency domain (Wiener, 1930). Compared to seismic interferometry (e.g., Wegler & Sens-Schönfelder, 2007), we choose relatively small time-windows because atmospheric properties change over short periods of time.

By definition, autocorrelation functions are symmetric; therefore, we only store the causal parts (≥0 s lag) for further processing. In addition, autocorrelation amplitudes quickly decay below noise levels for an increasing lag time, consequently we only keep the first 30 s.

### 3.2. Origin of the Infrasound Autocorrelation Codas at El Reventador

Before detailing the interferometry procedure, we investigate the origin of the coherent phases in the infrasound autocorrelation functions at El Reventador. In the literature, we find two models that explain the origin of the seismic autocorrelation codas. Wegler and Sens-Schönfelder (2007) interpret phases in the autocorrelation functions as backscattered and reflected waves of the zero offset Green's function, whereas Sánchez-Sesma et al. (2011) demonstrate that autocorrelation measures average seismic energy density and is proportional to the imaginary part of the Green's function. Here, to identify the origin of the infrasound autocorrelation codas, we apply array analysis to the autocorrelation functions computed at each microphone of the AZU array. We use the time delays between the autocorrelation functions to infer the direction of arrival of the phases in the coda (Figure 3a). Specifically, we divide the autocorrelation functions into 4-s consecutive windows overlapped 90% and compute the time delays between microphones using cross correlation. Subsequently, for each window, we find the slowness vector that better accounts for the time delays between array elements to ultimately obtain the back azimuth (e.g., Johnson et al., 2018; Matoza et al., 2007). We perform this process for autocorrelations stacked every 12 h between January 14 and July 22, 2015, totaling 190 days. Back azimuths from the autocorrelations show variable dispersion a function of lag time with the mean constrained from 0° to 18° and from 300° to 360° (Figure 3b). These directions correspond to the closest section of the horseshoe like caldera walls surrounding the volcano (Figures 1b and 2b), where likely direct waves are being reflected to the AZU array.

## 4. Results

### 4.1. Infrasound Relative Velocity Changes

Autocorrelation functions during the ~6.3-month period (Figures 4b and 4c) show temporal shifts between individual phases. For example, looking closer at the LAV and AZU autocorrelation functions, we observe that daily phase shifts are convolved with subdiurnal shifts (Figures 4d and 4e). Assuming those shifts are related to changes of the medium velocity ($c$), we apply trace-stretching to retrieve phase-arrival-time perturbations ($\Delta t$) that are related to velocity perturbations ($\Delta c$) as (Snieder et al., 2002):

$$-\frac{\Delta t}{t} = \frac{\Delta c}{\overline{c}} = \frac{c - \overline{c}}{\overline{c}} \tag{1}$$

where $t$ is the elapsed time in the autocorrelation coda and $\overline{c}$ is the average velocity. We follow a similar trace-stretching procedure to the one described in Mikesell et al. (2015) to retrieve the relative velocity change ($\Delta c/\overline{c}$) of the medium. Additionally, we acknowledge that trace-stretching can lead to spurious velocity changes due to frequency variability of the noise source (Zhan et al., 2013). However, scaling the Zhan et al. (2013) results to our set of parameters, we find that for frequencies of 1 Hz and lag times of at least seven periods in the autocorrelation coda, the effect of frequency variability on relative velocity change should be ~0.04%, which is 75 times smaller than our inferred typical relative change in sound speed (3%).

For AZU and LAV, the reference waveform required in the stretching method is chosen as the 6.3-month stack of the 15,770 autocorrelation functions, each of length 30 s (Figures 5a and 5c). After, we select lag times between 7 and 11 s and 11 and 26 s for AZU and LAV, respectively, to calculate the temporal velocity variations (in Section 4.2 is explained the rationale behind these choices). We find these lag times to better capture velocity changes due to changes in ambient air temperature. Thus, our results show that relative velocity changes are synchronous with temperature oscillations recorded separately in the data loggers (Figures 5b, 5d, and 5e). The temporal variations of $\Delta c/\overline{c}$ include higher-frequency variations superimposed on the lower-frequency diurnal variations; thus, to ease the comparison with temperature measurements, we apply a local regression model to retrieve the low-frequency component of the relative velocity changes.

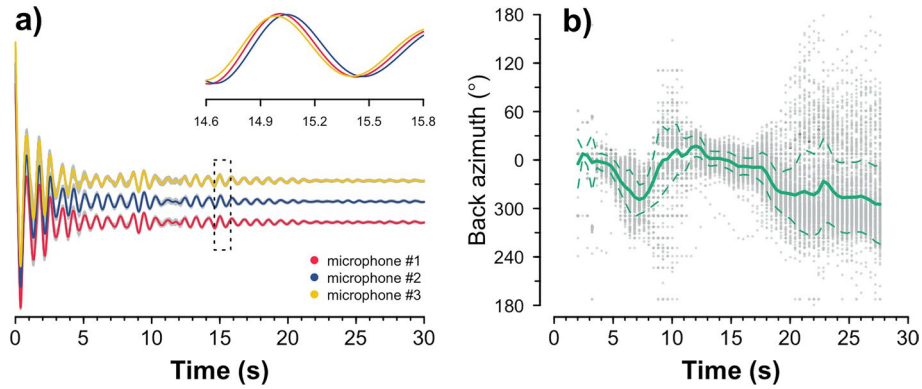


**Figure 3.** Array analysis of the autocorrelation functions. (a) Autocorrelation stacks from the three microphones installed at the AZU array. Looking closer for times between 14.6 and 15.8 s (dashed black box), we observe time delays between phases in the autocorrelations. (b) Back azimuth results of coherent phases detected in the autocorrelation codas. Each gray dot indicates the back azimuth of coherent phases detected in the autocorrelation codas as function of time. The average back azimuth (green) preferentially points to the proximal sections of the caldera walls of El Reventador. The green dashed lines indicate one standard deviation from the mean.

In particular, we use the LOESS regression approach (Cleveland et al., 1988) with a smoothing parameter $\alpha = 0.022$, which has the effect of filtering out frequencies higher than ~1 cycle/day. Hereafter, we refer to $(\Delta c/\overline{c})_{\text{low}}$ as this low-frequency component of $\Delta c/\overline{c}$.

### 4.2. Infrasound Inferred Temperatures

In the most general form $c\left(T,\vec{w}\right)$, the sound speed, is a function of the atmospheric temperature ($T$) and the wind velocity ($\vec{w}$) and can be approximated as (e.g., Garcés et al., 1998; Ortiz et al., 2018):

$$c\left(T,\vec{w}\right) = \sqrt{\gamma RT \,/\, M} + \vec{w}\cdot\hat{r} \tag{2}$$

where $\gamma$ is the adiabatic index, $R$ is the ideal gas constant, $M$ is the air molar mass, and $\vec{w}\cdot\hat{r}$ represents the projection of the wind velocity along the direction of propagation (wavefront normal) $\hat{r}$.

We demonstrate in Section 3.2 that autocorrelation codas at AZU are composed of waves reflected off the caldera walls and that the main direction of propagation of these reflected waves is close to the north-south direction. Additionally, from the continuous reports of Instituto Geofísico (www.igepn.edu.ec) about the plume drift and ash dispersals of Volcán El Reventador, we infer that winds in the area predominantly originate between the east-northeast and east-southeast directions. Wind directions that are consistent with the general air circulation at equatorial latitudes and with other wind observations in Ecuador (e.g., Ortiz et al., 2018; Wagemann et al., 2015). Thus, the influence of wind on phase shifts at AZU is likely low given the near perpendicular orientation between wind velocity and direction of propagation of reflected waves (i.e., $\vec{w}\cdot\hat{r} \sim 0$). Further, for the interferometry procedure, we select coherent phases between 7 and 11 s because of the larger back azimuth dispersion and the high signal-to-noise ratio (Figure 3). Larger back azimuth dispersion indicates that crosswinds are stronger for this portion of reflected waves, assuring that $\vec{w}$ and $\hat{r}$ are nearly perpendicular. At the same time, we expected that the direction between winds and the direction of propagation of reflected waves at LAV is also near perpendicular given the relative location of this station respect to the caldera walls. Consequently, separating the low-frequency component, $(\Delta c/\overline{c})_{\text{low}}$, of Equation 1 and neglecting the wind-speed term in Equation 2, we combine the equations to obtain:

$$T_i = \frac{\overline{c}^2 M}{\gamma R}\left[\left(\frac{\Delta c}{\overline{c}}\right)_{\text{low}} + 1\right]^2 \tag{3}$$

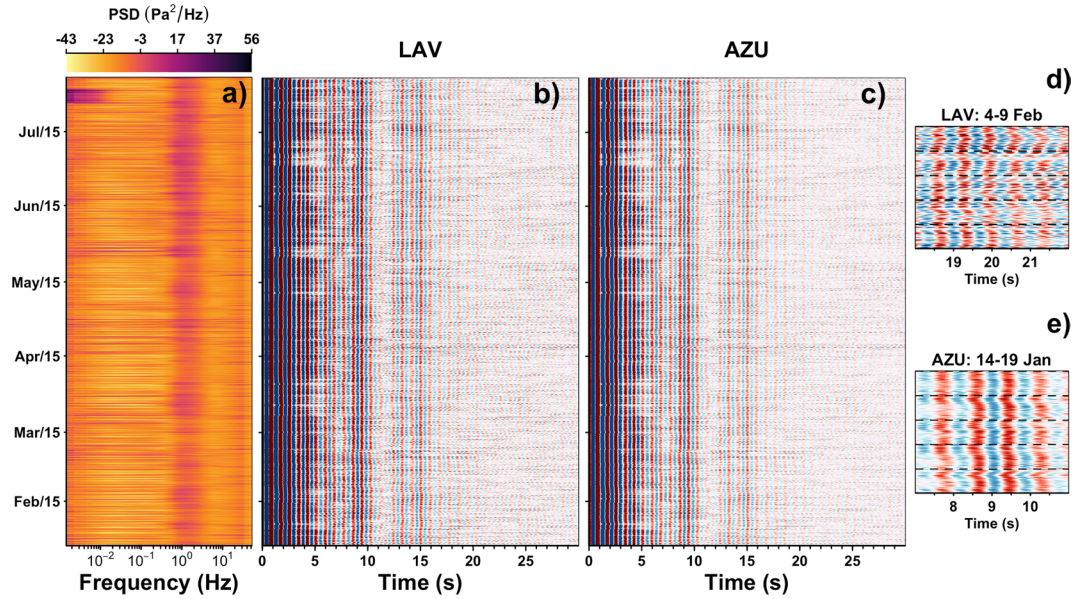


**Figure 4.** Power spectral density (PSD) and autocorrelation functions of infrasound records between January 14 and July 22, 2015. (a) The power spectral density for AZU microphone #2 shows that most of the energy is concentrated at frequencies between 1 and 2 Hz. (b) Causal part of autocorrelations computed using 2,048-s windows in the frequency band from 1 to 2 Hz for microphone #1 of LAV. (c) Similarly, autocorrelations for microphone #2 of AZU. (d) Close-up of (b) for February 4–9, 2015 between 18 and 22 s. (e) Close-up of (c) for January 14–19, 2015 between 7 and 11 s. Daily phase-arrival perturbations that are convolved with subdiurnal perturbations can be observed. Autocorrelations for microphones #1 and #3 of AZU are almost identical to the results shown in (c) and are presented in the supporting information (Figure S3).

where $T_i$ is the infrasound inferred temperature. Considering the average temperature registered in the AZU data logger for the time period January 14 to February 15, 2015, $T = 19.6$°C ($\overline{c} \sim 343.1$ m/s), we use Equation 3 to obtain the temperature time series. Infrasound inferred temperatures closely resemble ambient temperature cycles, with a clear diurnal periodicity (Figure 6a). Minimum and maximum temperatures are reached at ~10:30 a.m. and ~8:00 p.m. (UTC) (corresponding to 5:30 a.m. and 3:00 p.m. local time, respectively), which are consistent with the local sunrise and warmest time of the day, respectively. Usually, there is a lag of ~3 h between the solar noon and the time of maximum temperature. We expect this lag because afternoon incoming solar radiation still exceeds the outgoing heat energy from the surface of the Earth, resulting in an energy surplus that continuous to heat the atmosphere (Ahrens, 2008).

Similarly, considering the average temperature registered in the LAV data logger of 18.27°C ($\overline{c} \sim 342.3$ m/s), we obtain infrasound inferred temperatures using Equation 3 (Figure 6b). Although the amplitude of the infrasound inferred temperature is smaller than the data logger temperature, both time series are in phase.

It may be tempting to directly derive temperature from relative velocity changes, but in the general case the wind velocity ($\vec{w}$) and the direction of propagation ($\hat{r}$) of the reflected waves in the coda will not always be perpendicular, hence the effects of wind on $\Delta c/\overline{c}$ cannot be neglected. The lower sensitivity to winds of coherent phases in the AZU and LAV autocorrelations is fortuitous and it should be regarded as a special case at this field site. Hereafter, we only present comparative results between $(\Delta c/\overline{c})_{\text{low}}$ and temperatures for the additional stations. In the next subsection, we show that $(\Delta c/\overline{c})_{\text{low}}$ can also track variations of wind speeds.

We obtain $(\Delta c/\overline{c})_{\text{low}}$ time series following the procedure presented above for REVS (Figure 1b) as well as for P30M, R32K, and H17A stations from the TA (Figure S2) for different time periods, depending on data availability (Table S1). The results from these other stations also show daily synchrony between relative velocity changes and independently measured temperature fluctuations (Figures 7 and S4). The similarity between low-frequency relative velocity changes and temperatures is quantified using zero-lag cross cor-

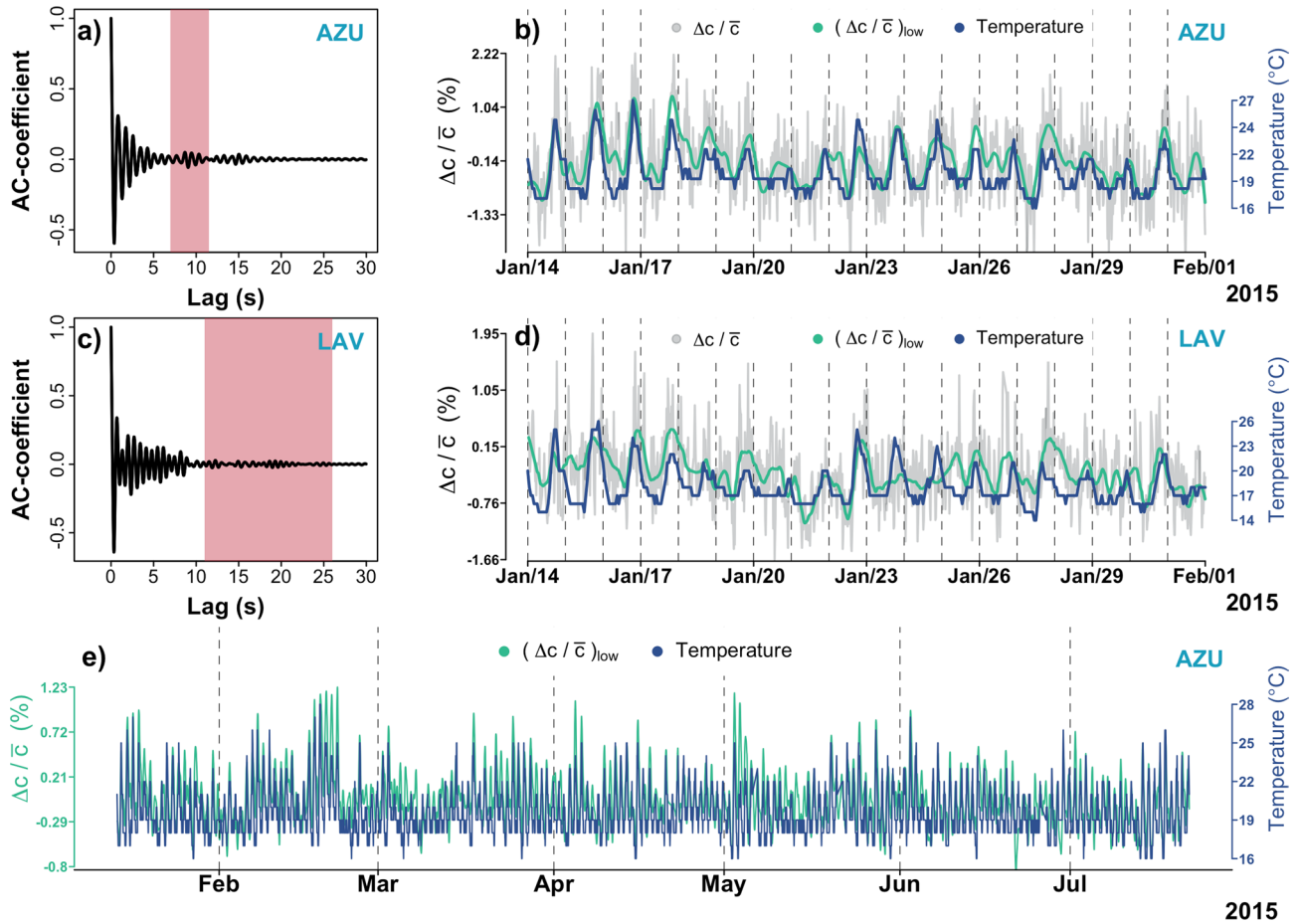


**Figure 5.** Autocorrelation stacks and relative velocity changes for AZU and LAV in the frequency band from 1 to 2 Hz. (a) Autocorrelation stack for AZU. For the stretching method, we find that lag times between 7 and 11 s (red shaded area) are more sensitive to velocity variations due to temperature changes. (b) The velocity perturbations (gray line) computed at AZU and their corresponding low-frequency component $(\Delta c/\overline{c})_{\text{low}}$ (green line) are compared to daily temperature cycles (blue line). (c) Autocorrelation stack for LAV. We choose lag times from 11 to 26 s (red shaded area) to compute the relative velocity changes, which are shown in (d). (e) Extended results for AZU from January 14 to July 22, 2015. Autocorrelation stacks and $\Delta c/\overline{c}$ time series for microphones #1 and #3 of AZU are shown in Figure S3 and are very similar to the results presented in (a) and (b) for microphone #2.

relation over 32 days for each station, with the limitation that correlation coefficients may be affected by offsets, long period trends, and different scaling factors between the time series (e.g., Figure 7). Estimated correlation coefficients are between 0.34 and 0.79, with AZU being the station with the highest correlation and H17A having the lowest correlation (Table 1). Furthermore, spectral analysis of unfiltered $\Delta c/\overline{c}$ reveals clear peaks at diurnal periods for all the stations, while semidiurnal peaks are more evident for AZU and REVS stations (Figures 6c–6h).

### 4.3. Effects of Wind on the Autocorrelation Infrasound Interferometry

We investigate the effects of wind on the interferometry results using data from the R32K station, because in addition to the infrasound sensor, it is equipped with dedicated wind and temperature sensors. We find that $(\Delta c/\overline{c})_{\text{low}}$ tracks well with both temperature and wind speed variations and occasionally $(\Delta c/\overline{c})_{\text{low}}$ only correlates with wind speed variations (Figure 7). We identify two time periods when $(\Delta c/\overline{c})_{\text{low}}$ is visually out-of-phase with temperature and better tracks wind speed changes: June 10–13, 2017 and June 15–18, 2017 (Figures 7b and 7c). As result the correlation coefficient between the low-frequency component of wind speed and $(\Delta c/\overline{c})_{\text{low}}$ is equal to 0.59, which is greater than the similarity between temperature and $(\Delta c/\overline{c})_{\text{low}}$. The low-frequency component of the wind speed is also computed using the LOESS approach with a smoothing parameter $\alpha = 0.022$. Similar out-of-phase correlations between $(\Delta c/\overline{c})_{\text{low}}$

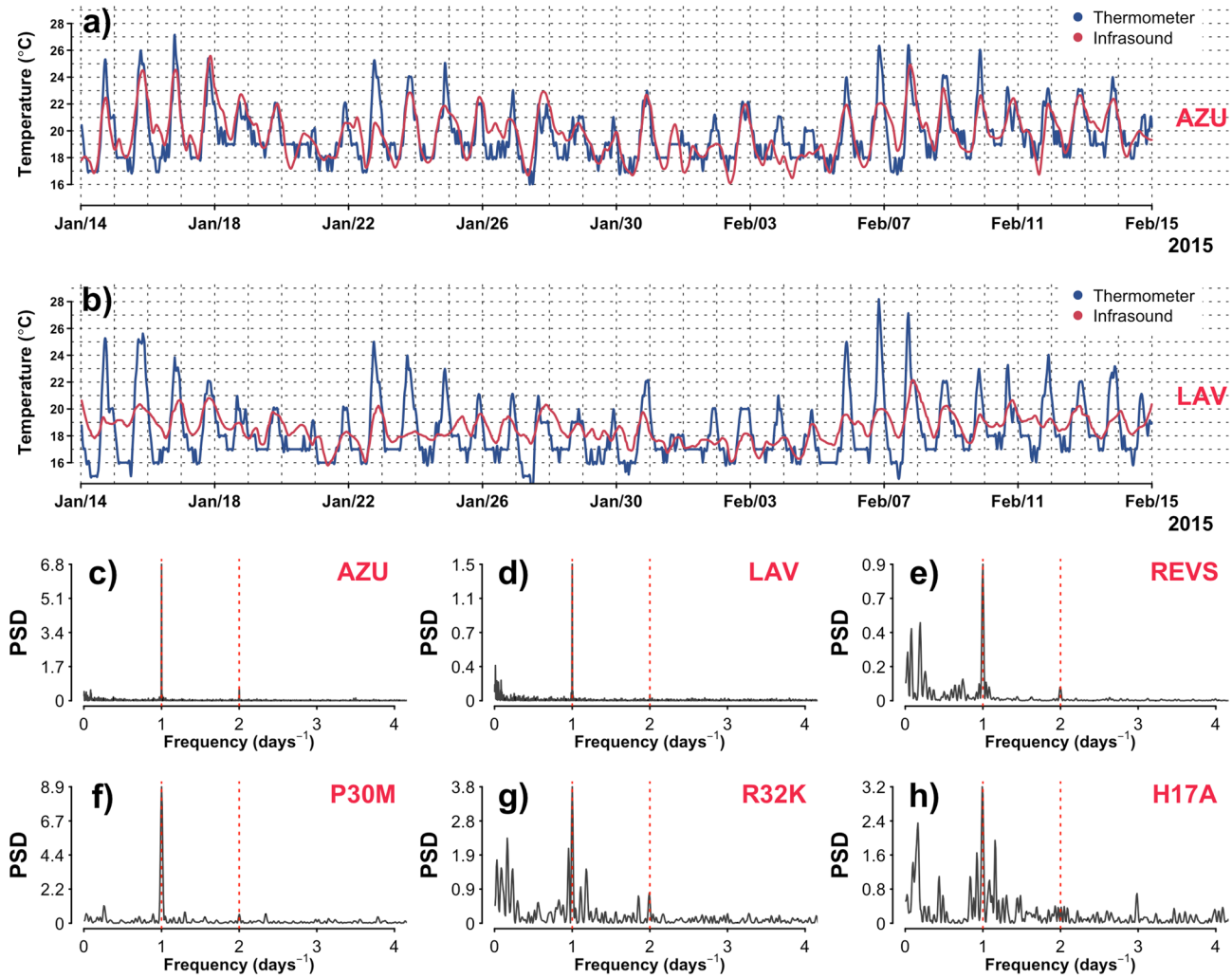


**Figure 6.** Infrasound inferred temperatures and spectral properties of the relative velocity changes. (a) Average temperatures (red line) obtained from the three independent single-sensor autocorrelations at AZU and temperatures collected by the corresponding digitizer probe (blue line) for the time period January 14 to February 15, 2015. (b) Infrasound inferred temperatures (red line) compared to the digitizer temperatures (blue line) at LAV. (c–h) Power spectral densities of the unfiltered relative velocity changes. The diurnal (at 1 days$^{-1}$) and semidiurnal (at 2 days$^{-1}$) peaks are marked with the red dashed lines.

and temperature can be observed at REVS and H17A in June 20–22, 2013 and in July 22–25, 2014, respectively (Figure S4). For scatter phases in the autocorrelation codas with paths ($\hat{r}$) near or parallel to $\vec{w}$, we may see more out-of-phase correlations between temperature and $(\Delta c/\overline{c})_{\text{low}}$ as well as corresponding correlation coefficients to drop because winds also play an important role in sound-speed changes. Wind speeds along the propagation direction of coherent phases linearly modify sound speeds, while only the square root of temperatures alter sounds speeds. Additionally, we examine the relation between wind and the convergence of the coherent phases in the autocorrelation functions. We calculate the correlation coefficients between phases in the reference waveform and each autocorrelation function for lag times from 1 to 15 s, as part of the stretching procedure. Every low-frequency relative velocity change computed at R32K is color coded to show the similarity between phases (Figure 7a). The 86% of the phases have a correlation coefficient of at least 0.8, which suggest that the convergence of the coherent phases is stable through time and is weakly affected by time-varying parameters such as the winds.

Lastly, we use temperature data recorded in the digitizer (Q330) and the weather station (WXT 520) to establish a temporal and spatial correspondence with the low-frequency relative velocity changes (Figures 7d and 7e). The weather station and infrasound sensors are located outdoors, whereas the digitizer is inside a

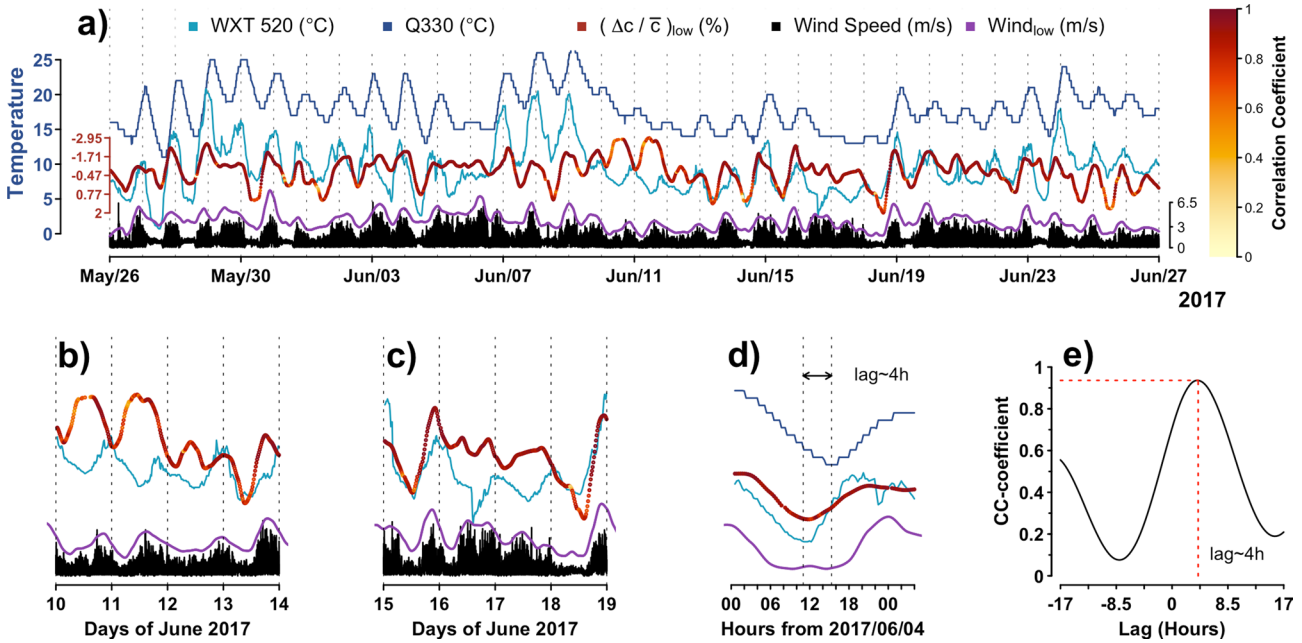


**Figure 7.** Comparison among digitizer—indoor—temperature (Q330), weather station—outdoor—temperature (WXT 520), $(\Delta c/\overline{c})_{low}$, and wind speed time series from the R32K station. (a) Time series from May 26 to June 27, 2017. Darker colors on $(\Delta c/\overline{c})_{low}$ indicate higher correlation coefficient between phases in the autocorrelation stack and individual autocorrelation functions for times between 1 and 15 s. (b, c) Examples where $(\Delta c/\overline{c})_{low}$ (red) better correlates with low-frequency wind speed (purple) variations rather than temperature variations (light blue). (d) Zoom in of the time series shown in (a) from 00:00 4 June to 04:00 5 June 2017. $(\Delta c/\overline{c})_{low}$ (red) and outdoor temperature (light blue) are synchronous, whereas between $(\Delta c/\overline{c})_{low}$ and indoor temperature (dark blue) there is a clear lag of ~4 h. (e) The cross-correlation function between outdoor and indoor temperature also confirms a lag time of 3.97 h, between these time series.

thermal vault (Tytell et al., 2016). Using cross correlation, we find that the lag time between outdoor temperature and $(\Delta c/\overline{c})_{low}$ is ~17 min, while the lag time between indoor temperature and $(\Delta c/\overline{c})_{low}$ is ~238 min (~4 h). Furthermore, the cross-correlation function between indoor and outdoor temperature also confirms that the lag time is 238 min (Figure 7e). Additionally, there is a clear difference between the average indoor and outdoor temperatures. We emphasize that these lags and temperature differences are unique to the R32K station configuration, consequently these observations are not applicable at the LAV or AZU stations. Because the time series have different lengths, we resample the data before computing cross correlations.

## 5. Discussion

Our autocorrelation infrasonic interferometry methodology appears to be robust and independent of the station configuration, geographical location, or time period. For instance, the REVS and AZU stations are ~3.8 km apart with an elevation difference of ~130 m and have different station configurations and time periods; nevertheless, the results from the proposed method track well the daily temperature oscillations at both stations. Likewise, low-frequency variations of $\Delta c/\overline{c}$ are in synchrony with temperature fluctuations for stations P30M, R32K, and H17A, which are in coastal and inland locations (Figure S2). P30M and H17A are in Southeast Alaska and H17A is in Yellowstone. Further, at the three microphones of AZU, we obtained almost identical interferometry results (Figure S3), which is expected as the microphones are spatially close, thereby indicating that the method is robust and repeatable.

We also demonstrate that low-frequency relative velocity changes can track wind speed variations. We mainly depict examples for the station R32K (Figures 7b and 7c), but wind effects on $(\Delta c/\overline{c})_{low}$ can also be seen

**Table 1**
*Correlation Coefficients Between Temperatures and Relative Velocity Changes*

| Station | Coefficient |
|---|---|
| AZU | 0.79 |
| LAV | 0.59 |
| REVS | 0.69 |
| P30M | 0.61 |
| R32K | 0.49 |
| H17A | 0.34 |

at REVS and H17A (Figures S4a and S4c). For autocorrelation codas composed of scatter phases with paths ($\hat{r}$) near or parallel to wind velocities ($\vec{w}$), we expect to see stronger influence of wind on $(\Delta c/\overline{c})_{\text{low}}$. This is because sound speed varies linearly with wind speeds and only with the square root of temperatures (Equation 2). Further, air circulation processes that can modify $(\Delta c/\overline{c})_{\text{low}}$ are daily wind-velocity changes that originate in mountain breezes (Ahrens, 2008) or in the evolution of the atmospheric boundary layer (Fee & Garcés, 2007; Matoza et al., 2009). Although $(\Delta c/\overline{c})_{\text{low}}$ contains wind velocity information, retrieving wind quantities from autocorrelation interferometry results is beyond the scope of this study because relating a vector field (wind velocity) with scalar sound speeds from a single microphone is not straightforward.

Serendipitously, the predominant winds at El Reventador are easterlies and the propagation paths of reflected waves in the autocorrelation codas are close to the north-south direction. Thus, wind effects (for the predominant wind direction in the area) on the relative velocity changes computed at AZU and LAV stations are presumably low because $\vec{w} \cdot \hat{r} \sim 0$ ($\vec{w}$ and $\hat{r}$ are nearly perpendicular). This geometry at El Reventador helps us to establish a direct relationship between temperatures and low-frequency relative velocity changes (Equation 3) and ultimately derive temperatures from the autocorrelation infrasound interferometry procedure. However, in general, the wind velocity ($\vec{w}$) and the direction of propagation ($\hat{r}$) of the reflected waves in the coda will not be perpendicular; therefore, wind effects cannot generally be neglected. Even small deviations between infrasound inferred temperatures and independent temperature records shown in Figures 6a and 6b may be explained by influence of wind velocity on $(\Delta c/\overline{c})_{\text{low}}$ (e.g., wind direction deviating from the inferred dominant easterly direction) and the inherent errors of the stretching method (Figure S5).

We also show that low-frequency relative velocity variations better track outdoor temperatures than temperatures recorded by digitizers that are located inside thermally insulated vaults (Figures 7d and 7e). For the R32K station, we find that lag times between outdoor temperatures and $(\Delta c/\overline{c})_{\text{low}}$ and the digitizer probe are ~17 and ~238 min, respectively. The 17 min are within the time resolution (50% window overlap) of the proposed method and we explain the 238 min as heat diffusion occurring over several hours through the vault that contains the digitizer. Additionally, there is a clear difference between the average indoor and outdoor temperatures (Figure 7a); we also explain this difference due to the thermal insulation provide by the vault. Moreover, local temperature effects at AZU should be milder as the digitizer is directly on the ground surface in a shaded area inside a plastic box that does not have as good thermal insulation, while local temperature effects at LAV should be a little stronger because the plastic box that contains the digitizer is on an open space with direct exposure to sunlight. We note that data logger temperatures at LAV are at least one or two degrees greater than peak-to-peak data logger temperatures at AZU (Figures 6a and 6b). These temperature differences can be explained by the direct exposure to sunlight of the LAV data logger or the presence of local thermal gradients.

Other deviations between infrasound inferred temperatures and probe temperatures may arise due to the nature of both measurements. Temperature probes provide point measurements, whereas infrasound provides an average measurement over a volume. This follows after acknowledging the origin of the infrasound autocorrelation codas, which are composed of waves reflected off the caldera walls at El Reventador (Figure 3). The horseshoe like caldera acts as a natural parabolic reflector, where direct waves from the waterfall may undergo several reflections. For instance, reflected waves arriving to AZU at $t \sim 9$ s (Figure 5a) are inferred to propagate an additional distance of $\overline{c}t \sim 3{,}088$ m. Considering the single-scattering model with colocated source and receiver proposed by Aki and Chouet (1975), the maximum sampled volume by the reflected waves is a hemisphere of radius of $\overline{c}t/2$ that encloses the sensor above the ground. Thereby, infrasound inferred temperatures may permit spatial sampling of the atmospheric temperature and potentially avoid sharp thermal gradients near the ground (Ahrens, 2008), which thermometers in weather stations may be sensitive to. Additionally, autocorrelation infrasound interferometry may permit the study of small-scale convective processes in the atmospheric boundary layer that can impact local infrasound propagation as reported by Kim et al. (2018) and Smink et al. (2019).

In previous work, multistation ambient-noise infrasonic interferometry used microbaroms as the primary infrasound source; however, we show that autocorrelation interferometry is possible with higher-frequency local continuous noise sources such as waterfalls and rivers. We find that the frequency band from 1 to 2 Hz, at all six stations considered, adequately retrieves the daily fluctuations of the atmospheric temperature and wind. This frequency band is presumably appropriate for local sound-speed variations because it has infra-

sound with wavelengths of ~170–340 m, corresponding to a typical atmospheric boundary layer height. Microbaroms are typically peaked at ~0.2 Hz with roll-off at high frequencies that sometimes can extend into the 1–2 Hz band (Matoza et al., 2013). However, our power spectral density results (Figures 4a and S6) clearly indicate that the spectrum in the 1–2 Hz band deviates from the microbarom spectrum and it is consistent with the signal level of the local waterfall, exceeding and dominating over any microbarom energy in this band. This is also consistent with PMCC array detections near El Reventador (Figures 2a and S1); the San Rafael waterfall is the primary infrasound source in the region at these frequencies. Stations P30M, R32K, and H17A are also located near rivers, but discriminating and locating infrasound sources is not possible because the stations only have one infrasound sensor.

The retrieved relative velocity changes also contain an apparent semidiurnal period at AZU and REVS that weakens for stations P30M, R32K, and H17A located in the northern hemisphere (Figures 6c–6h). The semidiurnal peak could arise as either (1) simply a harmonic of the dominant diurnal temperature and relative sound-speed variation (any nonperfectly sinusoidal oscillation contains higher order harmonics of the dominant frequency) or (2) a separate real physical semidiurnal ground-level atmospheric oscillation. At this stage, we cannot distinguish between these two explanations. However, we note that the presence of the semidiurnal oscillation is also similar to infrasound observations near Volcán Tungurahua, where volcano and microbarom wave travel times also show clear semidiurnal oscillations (Ortiz et al., 2017, 2018). In the atmosphere, forcing for semidiurnal oscillations originates at stratospheric altitudes by ozone heating during the atmospheric tide generation. Effects from atmospheric tides on surface weather (e.g., wind, pressure) were previously thought to be negligible, as it was presumed that these effects originating at high altitudes were unlikely to propagate downward to the surface (e.g., Green et al., 2012). However, recent climate models consider the propagation of semidiurnal oscillations from the stratosphere to the ground (Covey et al., 2011). It is possible that semidiurnal oscillations in infrasound propagation near the ground have not been widely documented because atmospheric tides are weak, or not well-defined, poleward of ±40° in the troposphere (Covey et al., 2011).

## 6. Conclusions

We highlight the potential of autocorrelation infrasound interferometry to retrieve atmospheric characteristics (Figures 4–7, S3, and S4). We obtain low-frequency variations of relative sound speed consistent with daily temperature and wind cycles. Results from selected stations in Ecuador and the US EarthScope TA indicate that this method is applicable for stations in volcanic, mountainous, and costal settings over different time-periods. For stations inside El Reventador caldera, we show that coherent phases in the autocorrelation codas correspond to waves reflected off the caldera walls. Autocorrelation infrasound interferometry can take advantage of high-frequency continuous noise sources such as waterfalls and rivers. However, our method needs to be tested in stations located near other ambient infrasound noise sources (e.g., surf, dams, and wind farms). Further developments with this method have the potential to quantify the strength of ground-level semidiurnal variations in temperature and wind velocity.

**Acknowledgments**
Data from the TA network were made freely available as part of the EarthScope USArray facility, operated by Incorporated Research Institutions for Seismology (IRIS) and supported by the National Science Foundation, under Cooperative Agreements EAR-1261681. We would like to express our gratitude to Jorge Córdova, Freddy Vásconez, and Wilson Enriquez for their help during the installation and servicing of the infrasound arrays in El Reventador. This work was funded by Proyectos de Investigación 2018 Pontificia Universidad Católica del Ecuador, Proyectos de Asistencia Técnica 2019 del Instituto Panamericano de Geografía e Historia, and NSF grants EAR-1847736 & EAR-1830976.

## Data Availability Statement

Data from the TA network were made freely available as part of the EarthScope USArray facility. Data for AZU, LAV, CON, and REVS stations are also available through the IRIS DMC with the temporary network code 6M (Ortiz & Johnson, 2013).

## References

Ahrens, C. D. (2008). Essentials of meteorology: An invitation to the atmosphere. *Thomson Learning*, *3*, 53–57.

Aki, K., & Chouet, B. (1975). Origin of coda waves: Source, attenuation, and scattering effects. *Journal of Geophysical Research*, *80*(23), 3322–3342. https://doi.org/10.1029/JB080i023p03322

Bensen, G. D., Ritzwoller, M. H., Barmin, M. P., Levshin, A. L., Lin, F., Moschetti, M. P., et al. (2007). Processing seismic ambient noise data to obtain reliable broad-band surface wave dispersion measurements. *Geophysical Journal International*, *169*(3), 1239–1260. https://doi.org/10.1111/j.1365-246X.2007.03374.x

Bonnefoy-Claudet, S., Cotton, F., & Bard, P. Y. (2006). The nature of noise wavefield and its applications for site effects studies: A literature review. *Earth-Science Reviews*, *79*, 205–227. https://doi.org/10.1016/j.earscirev.2006.07.004

Brenguier, F., Boué, P., Ben-Zion, Y., Vernon, F., Johnson, C. W., Mordret, A., et al. (2019). Train traffic as a powerful noise source for monitoring active faults with seismic interferometry. *Geophysical Research Letters*, *46*, 9529–9536. https://doi.org/10.1029/2019GL083438

Brenguier, F., Shapiro, N. M., Campillo, M., Ferrazzini, V., Duputel, Z., Coutant, O., & Nercessian, A. (2008). Towards forecasting volcanic eruptions using seismic noise. *Nature Geoscience*, *1*(2), 126–130. https://doi.org/10.1038/ngeo104

Campillo, M., & Paul, A. (2003). Long-range correlations in the diffuse seismic coda. *Science*, *299*, 547–549. https://doi.org/10.1126/science.1078551

Cansi, Y. (1995). An automatic seismic event processing for detection and location: The P.M.C.C. method. *Geophysical Research Letters*, *22*(9), 1021–1024. https://doi.org/10.1029/95GL00468

Cleveland, W. S., Devlin, S. J., & Grosse, E. (1988). Regression by local fitting: Methods, properties, and computational algorithms. *Journal of Ecometrics*, *37*(1), 87–114. https://doi.org/10.1016/0304-4076(88)90077-2

Covey, C., Dai, A., Marsh, D., & Lindzen, R. (2011). The surface-pressure signature of atmospheric tides in modern climate models. *Journal of the Atmospheric Sciences*, *68*, 495–514. https://doi.org/10.1175/2010JAS3560.1

Donn, W. L., & Rind, D. H. (1972). Microbaroms and the temperature and wind of the upper atmosphere. *Journal of the Atmospheric Sciences*, *29*, 156–172. https://doi.org/10.1175/1520-0469(1972)029<0156:MATTAW>2.0.CO;2

Fee, D., & Garcés, M. (2007). Infrasonic tremor in the diffraction zone. *Geophysical Research Letters*, *34*, L16826. https://doi.org/10.1029/2007GL030616

Fricke, J. T., Evers, L. G., Smets, P. S. M., Wapenaar, K., & Simons, D. G. (2014). Infrasonic interferometry applied to microbaroms observed at the large aperture infrasound array in the Netherlands. *Journal of Geophysical Research*, *119*, 9654–9665. https://doi.org/10.1002/2014JD021663

Garcés, M., Hansen, R. A., & Lindquist, K. G. (1998). Traveltimes for infrasonic waves propagating in a stratified atmosphere. *Geophysical Journal International*, *135*, 255–263. https://doi.org/10.1046/j.1365-246X.1998.00618.x

Green, D. N., Matoza, R. S., Vergoz, J., & Le Pichon, A. (2012). Infrasonic propagation from the 2010 Eyjafjallajökull eruption: Investigating the influence of stratospheric solar tides. *Journal of Geophysical Research*, *117*, D21202. https://doi.org/10.1029/2012JD017988

Haney, M. M. (2009). Infrasonic ambient noise interferometry from correlations of microbaroms. *Geophysical Research Letters*, *36*, L19808. https://doi.org/10.1029/2009GL040179

Hobiger, M., Wegler, U., Shiomi, K., & Nakahara, H. (2014). Single-station cross-correlation analysis of ambient seismic noise: Application to stations in the surroundings of the 2008 Iwate–Miyagi Nairiku earthquake. *Geophysical Journal International*, *198*(1), 90–109. https://doi.org/10.1093/gji/ggu115

Johnson, J. B. (2006). Waterfall Infrasound. *Inframatics*, *13*(1), 1–10. https://www.scirp.org/journal/inframatics/

Johnson, J. B., Arechiga, R. O., Thomas, R. J., Edens, H. E., Anderson, J., & Johnson, R. (2011). Imaging thunder. *Geophysical Research Letters*, *38*, L19807. https://doi.org/10.1029/2011GL049162

Johnson, J. B., Lees, J. M., & Yepes, H. (2006). Volcanic eruptions, lightning, and a waterfall: Differentiating the menagerie of infrasound in the Ecuadorian jungle. *Geophysical Research Letters*, *33*, L06308. https://doi.org/10.1029/2005GL025515

Johnson, J. B., Ruiz, M. C., Ortiz, H. D., Watson, L. M., Viracucha, G., Ramon, P., & Almeida, M. (2018). Infrasound tornillos produced by Volcán Cotopaxi's deep crater. *Geophysical Research Letters*, *45*, 5436–5444. https://doi.org/10.1029/2018GL077766

Kim, K., Rodgers, A., & Seastrand, D. (2018). Local infrasound variability related to in situ atmospheric observation. *Geophysical Research Letters*, *45*, 2954–2962. https://doi.org/10.1002/2018GL077124

Landès, M., Ceranna, L., Le Pichon, A., & Matoza, R. S. (2012). Localization of microbarom sources using the IMS infrasound network. *Journal of Geophysical Research*, *117*, D06102. https://doi.org/10.1029/2011JD016684

Longuet-Higgins, M. (1950). A theory of the origin of microseisms. *Philosophical Transactions of the Royal Society A*, *243*, 137–171. https://doi.org/10.1098/rsta.1950.0012

Marcillo, O., Johnson, J. B., & Hart, D. (2012). Implementation, characterization, and evaluation of an inexpensive low-power low-noise infrasound sensor based on a micro-machined differential pressure transducer and a mechanical filter. *Journal of Atmospheric and Oceanic Technology*, *29*(9), 1275–1284. https://doi.org/10.1175/JTECH-D-11-00101.1

Matoza, R. S., Garces, M. A., Chouet, M. A., D'Auria, L., Hedlin, M. A. H., De Groot-Hedlin, C., & Waite, G. P. (2009). The source of infrasound associated with long-period events at Mount St. Helens. *Journal of Geophysical Research*, *114*, B04305. https://doi.org/10.1029/2008JB006128

Matoza, R. S., Hedlin, M. A. H., & Garces, M. A. (2007). An infrasound array study of Mount St. Helens. *Journal of Volcanology and Geothermal Research*, *160*, 249–262. https://doi.org/10.1016/j.jvolgeores.2006.10.006

Matoza, R. S., Landès, M., Le Pichon, A., Ceranna, L., & Brown, D. (2013). Coherent ambient infrasound recorded by the International Monitoring System. *Geophysical Research Letters*, *40*, 429–433. https://doi.org/10.1029/2012GL054329

Mikesell, T. D., Malcolm, A. E., Yang, D., & Haney, M. M. (2015). A comparison of methods to estimate seismic phase delays: Numerical examples for coda wave interferometry. *Geophysical Journal International*, *202*(1), 347–360. https://doi.org/10.1093/gji/ggv138

Ortiz, H. D., & Johnson, J. B. (2013). *Multi-year infrasound deployment at Volcán El Reventador [Data set]*. International Federation of Digital Seismograph Networks. https://doi.org/10.7914/SN/6M_2013

Ortiz, H. D., Johnson, J. B., Anzieta, J. C., Matoza, R. S., Anderson, F. J., Vallejo, S., et al. (2019). Overview of Reventador infrasound activity: From January 2015 to June 2019. *Abstract V44B-06 presented at 2019 Fall Meeting, San Francisco, CA*, 9–13 December.

Ortiz, H. D., Johnson, J. B., Ramón, P. G., & Ruiz, M. C. (2018). Using infrasound waves to monitor tropospheric weather and crater morphology changes at Volcán Tungurahua, Ecuador. *Journal of Volcanology and Geothermal Research*, *349*, 205–216. https://doi.org/10.1016/j.jvolgeores.2017.11.001

Ortiz, H. D., Matoza, R. S., Garapaty, C., Rose, K., Ramón, P., & Ruiz, M. C. (2020). Multi-year regional infrasound detection of Tungurahua, El Reventador, and Sangay volcanoes in Ecuador from 2006 to 2013. *Proceedings of Meetings on Acoustics*, *41*, 022003. https://doi.org/10.1121/2.0001362

Ortiz, H. D., Mikesell, D., Palacios, P., Anderson, J., & Anzieta, J. (2017). Semidiurnal effects on infrasound wave propagation at local distances. *Abstract S44A-06 presented at 2017 Fall Meeting, New Orleans, LA*, 11–15 December.

Roux, P., & Kuperman, W. A. (2004). Extracting coherent wave fronts from acoustic ambient noise in the ocean. *Journal of the Acoustical Society of America*, *116*(4), 1995–2003. https://doi.org/10.1121/1.1797754

Sánchez-Sesma, F. J., Rodríguez, M., Iturrarán-Viveros, U., Luzón, F., Campillo, M., Margerin, L., et al. (2011). A theory for microtremor H/V spectral ratio: Application for a layered medium. *Geophysical Journal International*, *186*(1), 221–225. https://doi.org/10.1111/j.1365-246X.2011.05064.x

Sens-Schönfelder, C., & Wegler, U. (2006). Passive image interferometry and seasonal variations of seismic velocities at Merapi Volcano, Indonesia. *Geophysical Research Letters*, *33*, L21302. https://doi.org/10.1029/2006GL027797

Shapiro, N. M., & Campillo, M. (2004). Emergence of broadband Rayleigh waves from correlations of the ambient seismic noise. *Geophysical Research Letters*, *31*, L07614. https://doi.org/10.1029/2004GL019491

Siderius, M., Harrison, C. H., & Porter, M. B. (2006). A passive fathometer technique for imaging seabed layering using ambient noise. *Journal of the Acoustical Society of America*, *120*, 1315–1323. https://doi.org/10.1121/1.2227371

Smink, M. M. E., Assink, J., Bosveld, F., Smets, P., & Evers, L. (2019). A three-dimensional array for the study of infrasound propagation through the atmospheric boundary layer. *Journal of Geophysical Research: Atmospheres*, *124*, 9299–9313. https://doi.org/10.1029/2019JD030386

Snieder, R., Grêt, A., Douma, H., & Scales, J. (2002). Coda wave interferometry for estimating nonlinear behavior in seismic velocity. *Science*, *295*, 2253–2255. https://doi.org/10.1126/science.1070015

Tytell, J., Vernon, F., Hedlin, M., Hedlin, C. D. G., Reyes, J., Busby, B., et al. (2016). The USArray Transportable Array as a platform for weather observation and research. *Bulletin of the American Meteorological Society*, *97*(4), 603–619. https://doi.org/10.1175/BAMS-D-14-00204.1

Wagemann, J., Thies, B., Rollenbeck, R., Peters, T., & Bendix, J. (2015). Regionalization of wind-speed data to analyse tree-line wind conditions in the eastern Andes of southern Ecuador. *Erdkunde*, *69*(1), 3–19.

Wapenaar, K., Draganov, D., Snieder, R., Campman, X., & Verdel, A. (2010). Tutorial on seismic interferometry: Part 1. Basic principles and applications. *Geophysics*, *75*(5), 75A195–75A209. https://doi.org/10.1190/1.3457445

Waxler, R., & Gilbert, K. E. (2006). The radiation of atmospheric microbaroms by ocean waves. *Journal of the Acoustical Society of America*, *119*(5), 2651–2664. https://doi.org/10.1121/1.2191607

Weaver, R. L., & Lobkis, O. I. (2001). Ultrasonics without a source: Thermal fluctuation correlation at MHz frequencies. *Physical Review Letters*, *87*, 134301. https://doi.org/10.1103/PhysRevLett.87.134301

Weaver, R. L., & Lobkis, O. I. (2002). On the emergence of the Green's function in the correlations of a diffusive field: Pulse-echo using thermal phonons. *Ultrasonics*, *40*, 435–439. https://doi.org/10.1016/S0041-624X(02)00156-7

Wegler, U., & Sens-Schönfelder, C. (2007). Fault zone monitoring with passive image interferometry. *Geophysical Journal International*, *168*, 1029–1033. https://doi.org/10.1111/j.1365-246X.2006.03284.x

Wiener, N. (1930). Generalized harmonic analysis. *Acta Mathematica*, *55*, 117–258. https://doi.org/10.1007/BF02546511

Zhan, Z., Tsai, V., & Clayton, R. (2013). Spurious velocity changes caused by temporal variations in ambient noise frequency content. *Geophysical Journal International*, *194*(3), 1574–1581. https://doi.org/10.1093/gji/ggt170

## Reference From the Supporting Information

Weaver, R. L., Hadziioannou, C., Larose, E., & Campillo, M. (2011). On the precision of noise correlation interferometry. *Geophysical Journal International*, *185*, 1384–1392. https://doi.org/10.1111/j.1365-246X.2011.05015.x